Impulsive enhancements of oxygen ions during substorms.

Mei-Ching Fok, Thomas E. Moore, Pontus C. Brandt, Dominique C. Delcourt, Steven P. Slinker, Joel A. Fedder

Impulsive enhancements of oxygen ions during substorms

Mei-Ching Fok,[1] Thomas E. Moore,[1] Pontus C. Brandt,[2] Dominique C. Delcourt,[3] Steven P. Slinker,[4] and Joel A. Fedder[5]

Received 9 May 2006; revised 14 July 2006; accepted 7 August 2006; published 20 October 2006.

[1] It has been observed that H^+ is the dominant ion species in the plasma sheet and the ring current during quiet times. However, the O^+/H^+ density ratio increases with increasing geomagnetic storm and substorm activity. Energetic neutral atom (ENA) images from Imager for Magnetopause-to-Aurora Global Exploration/High Energy Neutral Atom (IMAGE/HENA) reveal the rapid increase of O^+ ring current at substorm expansion. Finding the cause of this substorm-associated O^+ enhancement is the main focus of this paper. Two possible sources are suggested: direct injection from the ionosphere and energization of the preexisting oxygen ions in the magnetosphere. We perform numerical simulations to examine these two mechanisms. Millions of O^+ are released from the auroral region during a simulated substorm by the Lyon-Fedder-Mobarry MHD model. The subsequent trajectories of these outflowing ions are calculated by solving the full equation of particle motion. A few minutes into the substorm expansion phase, an enhancement in O^+ pressure is found on the nightside at $\sim$12 R_E. After careful analysis, we conclude that this pressure peak is coming from energization of the preexisting O^+ in the plasma sheet. The direct injection mechanism will introduce a significant time lag between strong ionospheric outflow and magnetospheric enhancement, so that it cannot explain the observed O^+ bursts. Using the temperature and density established by the test-particle calculations as boundary conditions to a ring current model, we calculate the O^+ fluxes and the corresponding ENA emissions during the model substorm. We are able to reproduce observable features of oxygen ENA enhancements as seen by IMAGE/HENA.

Citation: Fok, M.-C., T. E. Moore, P. C. Brandt, D. C. Delcourt, S. P. Slinker, and J. A. Fedder (2006), Impulsive enhancements of oxygen ions during substorms, *J. Geophys. Res.*, *111*, A10222, doi:10.1029/2006JA011839.

1. Introduction

[2] Oxygen ion is one of the major ion species in the plasma sheet and ring current regions that bears many important and unique features. Unlike magnetospheric H^+, which originate from both the solar wind and the ionosphere, O^+ exclusively originate from the ionosphere [*Moore and Delcourt*, 1995; *Moore et al.*, 2001; T. E. Moore and J. L. Horwitz, Solar ablation of planetary atmospheres, submitted to *Reviews of Geophysics*, 2006]. Oxygen ions thus act as tracers of ionospheric influences on the magnetosphere. The upward flow of ionospheric O^+ is primarily from the auroral zone and is powered by solar wind energy dissipated into the ionosphere [*Moore et al.*, 1999, 2006]. The outflow and heating of O^+ alters the density, pressure, and ion composition in the magnetosphere. Since the lifetimes are different for different ion species, the composition changes in the magnetosphere control the recovery timescale of a magnetic storm. *Hamilton et al.* [1988] suggested the short charge exchange lifetimes of 75–100 keV O^+ are responsible for the rapid initial recovery of the major storm on 8–9 February 1986. These O^+ ions can also cause the reduction of reconnection rate by decreasing of the Alfven speed or reduction of the convection strength by momentum conservation [*Winglee et al.*, 2002]. Owing to the relatively large gyroradius and small cyclotron frequency, O^+ ions behave nonadiabatically in much of the magnetosphere, especially near the central plasma sheet and during magnetic reconfiguration. Enhanced density of these heavy ions in the plasma sheet may lead to tearing mode instabilities and triggering substorm onset [*Baker et al.*, 1982, 1985] since the growth rate of tearing mode instability increases when the ratio of the ion gyroradius to the characteristic plasma sheet thickness rises.

[3] The energy density ratio of O^+/H^+ in the magnetosphere is small during quiet times; however, this ratio increases with increasing geomagnetic activity [*Young et al.*, 1982; *Hamilton et al.*, 1988; *Roeder et al.*, 1996; *Daglis*, 1997]. In large magnetic storms, O^+ becomes the dominant ion species. During extreme events, like the Halloween

[1]NASA Goddard Space Flight Center, Greenbelt, Maryland, USA.
[2]Johns Hopkins University Applied Physics Laboratory, Laurel, Maryland, USA.
[3]Observatoire de Saint-Maur, Centre d'Etude des Environnements Terrestre et Planétaires, Saint-Maur des Fosses, France.
[4]Naval Research Laboratory, Washington, D.C., USA.
[5]Leading Edge Technology, Inc., Alexandria, Virginia, USA.

0148-0227/06/2006JA011839

storm in October 2003, the O^+/H^+ energy density ratio is as high as 10–20 [*Nose et al.*, 2005]. It is apparent that, compared to H^+, the source and energization of O^+ are more responsive to storm activity, which is driven by disturbed solar wind conditions.

[4] The O^+ abundance in the magnetosphere is also sensitive to substorm activity. Using data from AMPTE/IRM, *Mobius et al.* [1987] found, after a substorm onset, flux increase in energetic (10–230 keV/e) ions in the plasma sheet and hardening of the energy spectra that are most pronounced for O^+. *Daglis and Axford* [1996] also found rapid enhancement of O^+ fluxes in the inner magnetotail after substorm onset. From the images taken by the Imager for Magnetopause-to-Aurora Global Exploration/High Energy Neutral Atom (IMAGE/HENA) imager, *Mitchell et al.* [2003] found intense oxygen (52–180 keV) energetic neutral atom (ENA) bursts at each substorm onset. In contrast, there were weak responses in hydrogen ENA at similar energies. They suggested that the nonadiabatic acceleration of O^+ during dipolarization is responsible for the observed oxygen bursts seen by IMAGE/HENA. This mechanism was previously proposed and modeled by *Delcourt* [2002]. Another possible source of the substorm oxygen bursts is direct injection of energetic O^+ from the ionosphere [*Sheldon et al.*, 1998].

[5] A simulation study was performed by *Moore et al.* [2005], of the formation of ring current from both solar and ionospheric plasmas. They used test-particle motions in magnetospheric fields from the magnetohydrodynamic (MHD) simulation of Lyon, Fedder, and Mobarry [*Fedder et al.*, 1995; *Mobarry et al.*, 1996; *Slinker et al.*, 2001]. They chose a state reflecting steady substorm growth conditions. Particles are initiated in regions representative of the solar wind proton source upstream of the bow shock, the polar wind proton source, and the auroral zone enhanced outflows of O^+, which is named "auroral wind." *Moore et al.* [2005] found that solar wind protons enter the ring current principally via the dawn flank, bypassing the energization processes in the midnight plasma sheet, while polar wind protons and auroral wind O^+ enter the ring current through the lobes and midnight plasma sheet. Since solar wind and ionospheric ions take different paths to the magnetosphere, they are expected to respond differently to substorm dynamics in the magnetotail and experience different energization along their trajectories. In this paper, we extend the work of *Moore et al.* [2005] in two ways. First, instead of steady magnetospheric conditions, protons and O^+ are released from their source regions during an MHD substorm cycle. Second, we extend the simulation into the inner magnetosphere using the Comprehensive Ring Current Model (CRCM) [*Fok et al.*, 2001]. The outflowing O^+ flux and energy are parameterized by instantaneous MHD density, Joule heating and field-aligned potential drop [*Strangeway et al.*, 2005]. The main focuses of this paper are to test the two candidate mechanisms (nonadiabatic energization versus direct injection) responsible for O^+ enhancements and to understand why protons and O^+ behave differently in substorms. As in the work of *Moore et al.* [2005], ion trajectories are calculated by the test-particle code of *Delcourt et al.* [1993, 1994] in the Lyon-Fedder-Mobarry (LFM) electric and magnetic fields. With each ion assigning a source flux, the density and pressure contributed by these ions in the magnetosphere are established. With these temperature and density as boundary conditions to the CRCM, we calculate the O^+ fluxes in the inner magnetosphere and the corresponding ENA emissions during the model substorm. Our simulated oxygen ENA images are compared with those from IMAGE/HENA. In the following sections, we will present some HENA observations of oxygen ENA, the details of our calculation, simulation results, and how we identify the source mechanisms for the impulsive increase of oxygen ions during substorms.

2. HENA Observations

[6] HENA obtains hydrogen and oxygen ENA images in the 10–198 keV and 52–264 keV ranges, respectively. Particles enter the fan shaped outer collimators that are electrostatically charged so that any charged particles below a specified energy are swept away into the collimators and are prevented from entering the system. The remaining ENAs and photons enter a thin slit covered with a front foil. The front foil decreases the photon intensity and the penetrating ENAs create a shower of electrons that are detected by a start microchannel plate (MCP) along the slit. This electron shower acts as the start pulse, triggering a time of flight (TOF) system. The ENAs continue with a scattering angle, which depends on particle velocity, and hits the stop MCP. There, the time of the stop pulse is similarly recorded by the MCP, and its two-dimensional (2-D) location is determined by position-sensitive anodes. The position of an ENA in the front-foil and the 2-D position on the stop MCP can now be used to compute the direction of the incoming ENA. In this way the angular resolution only depends on what angular bin size is chosen in the on board software. The angular resolution is $6^\circ \times 6^\circ$ for hydrogen with energy less than 60 keV and for oxygen. The resolution for hydrogen greater than 60 keV is $3^\circ \times 3^\circ$. The scattering in the front foil is velocity dependent and determines the point-spread function (PSF) of HENA. For a hydrogen the point-spread full width at half maximum is about 15° for 30 keV hydrogen and about 5° for 100 keV hydrogen. Owing to velocity dependence, the spread is larger for oxygen: $\sim 25^\circ$ for 100 keV oxygen and $\sim 10^\circ$ for 200 keV oxygen. A more detailed description of the HENA instrument can be found in the work of *Mitchell et al.* [2000].

[7] The oxygen ENA signal during substorms is one of the most outstanding features in the HENA data set [*Mitchell et al.*, 2003]. At each storm-time substorm onset a significant increase of the oxygen ENA intensities can be seen coming from the nightside and low altitudes. The increase lasts for about 20–30 min and then decays away on similar timescales. While the overall hydrogen intensity is higher than the oxygen intensity, the relative intensity variation of the hydrogen ENA signal is much more gradual. Figure 1 summarizes the HENA observations of the substorm injection of 28 October 2001. The upper row displays the oxygen ENA images in the 96–180 keV range, the second row 27–39 keV hydrogen, and the third row 60–119 keV hydrogen. All ENA images were obtained with a 4-min integration. Dipole field lines of *L*-shells 4 and 8 are plotted at four local times for reference. IMAGE was in the Northern Hemisphere on the nightside for all images.

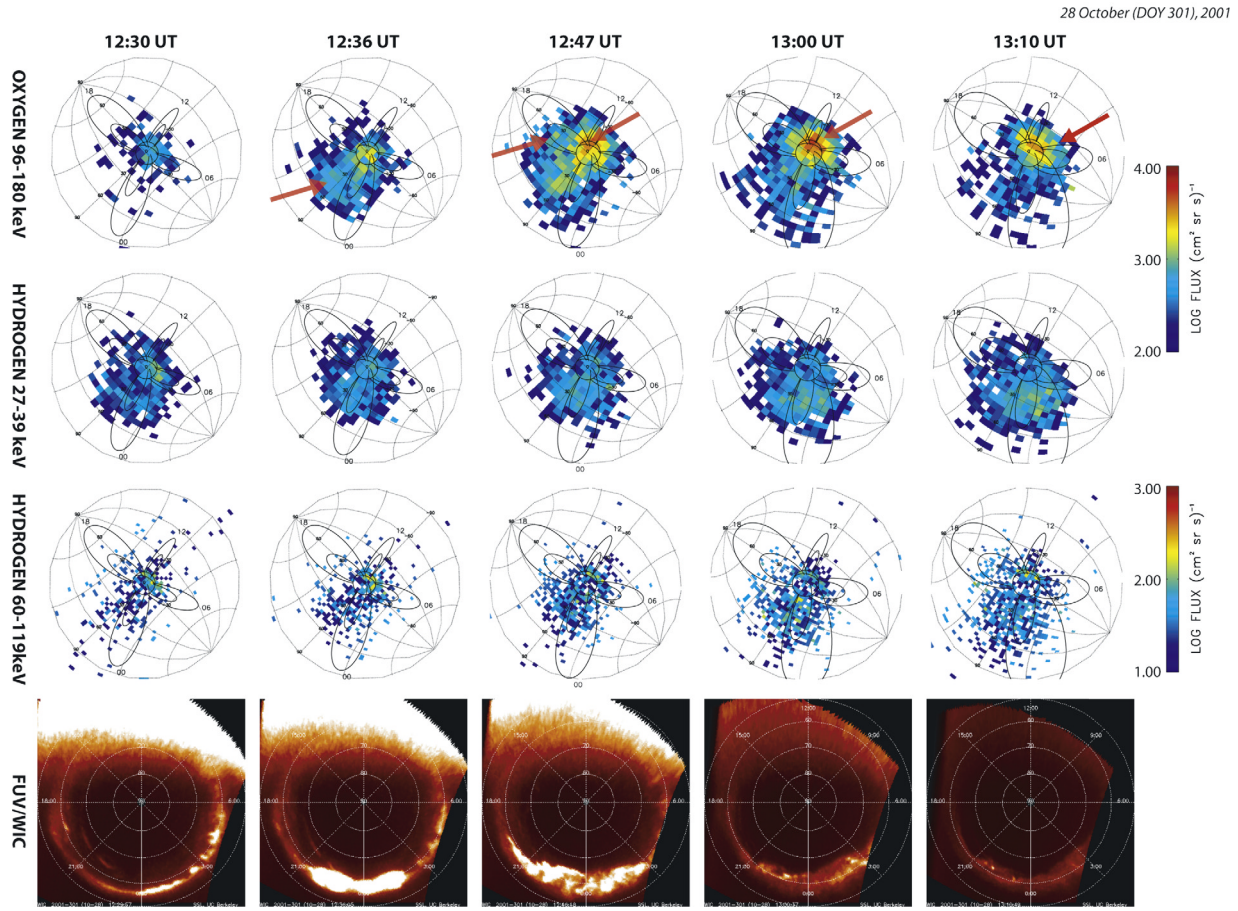

Figure 1. Summary of the High Energy Neutral Atom (HENA) observations starting at 1230 UT on 28 October 2001 for hydrogen and oxygen. Red arrows show oxygen injection, subsequent low-altitude ENA emissions, drift around, and decay. Bottom row shows the Far Ultraviolet (FUV) Wide Imaging Camera (WIC) auroral images projected in magnetic coordinates.

The bottom row shows the auroral images simultaneously obtained by the Far Ultraviolet (FUV) Wide Imaging Camera (WIC) onboard IMAGE [*Mende et al.*, 2000]. The substorm onset was seen at 1236 UT. Note that the high-altitude intensification in the oxygen image indicated by the red arrow. A slight increase is also visible on the high-altitude nightside in the hydrogen ENA images, but it is much more gradual.

[8] At 1247 UT, an increase in the oxygen intensity at high altitudes is seen together with strong emissions at low altitudes. We interpret this low-altitude enhancement as coming from the nearly mirroring oxygen ions and the subsequent interaction with the upper atmosphere [*Roelof*, 1997]. High-altitude oxygen emissions have now spread to the duskside consistent with the direction of curvature-gradient drift. There is only a slight enhancement at low altitudes in the hydrogen images. Note also that the hydrogen enhancement for the 27–39 keV range appears in the midnight-dawn sector, consistent with electric drifts in a skewed electric potential pattern as observed by *Brandt et al.* [2002] and successfully modeled by *Fok et al.* [2003] and *Ebihara and Fok* [2004].

[9] At 1300 UT, the high-altitude oxygen emissions have decreased and the low-altitude component of the oxygen emissions appears to have moved over to the dayside. Later at 1310 UT, the oxygen emissions spread even further into the dayside. On the other hand, the hydrogen emissions display a continuous increase on the nightside with some increase around dusk during the substorm recovery, owning to the enhanced convection. This gradual increase in hydrogen cannot be attributed to the decreasing distance of the IMAGE satellite to the source region. The reason is that the pixel size is much smaller than the extent of the source region. Only when the source can be considered as a point source, then the intensity falls off as $1/r^2$. As the source extent grows the exponent in the denominator comes closer to zero. For these HENA images the ring current source is much large than the pixel size and therefore intensity does not vary with distance.

3. Simulations

3.1. LFM Substorm During a IMF Southward Turning

[10] The LFM model used in this study is described in detail by *Fedder et al.* [1995], *Mobarry et al.* [1996], and *Slinker et al.* [1998]. The model solves the ideal MHD equations in a distorted spherical grid that extends 24 Earth radii (R_E) sunward of the Earth to 300 R_E tailward and 90 R_E in the Y and Z direction. The inner boundary is a sphere with a radius of 3.2 R_E centered on the Earth. Field-aligned

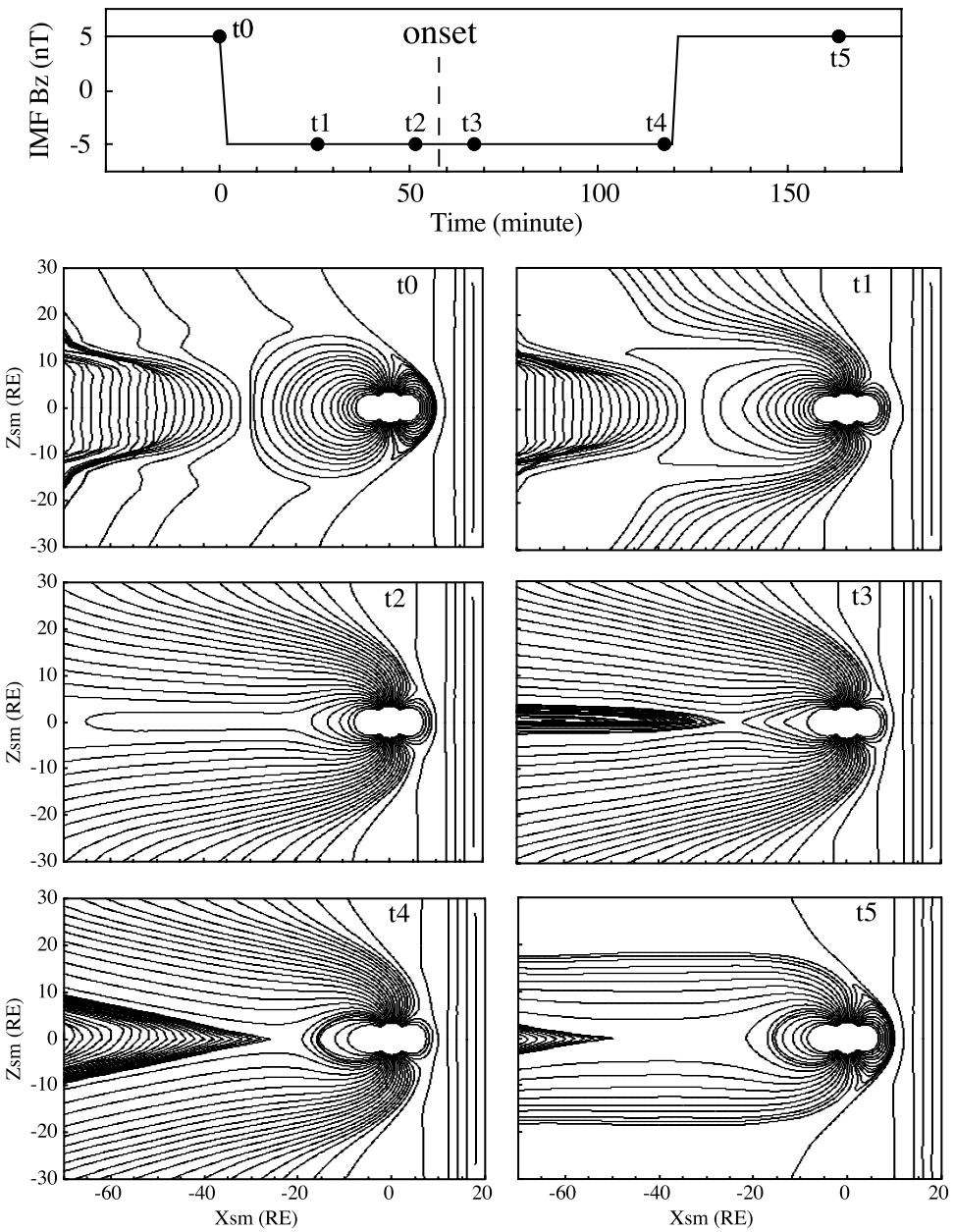

Figure 2. Input interplanetary magnetic field (IMF) Bz as a function of time for the Lyon-Fedder-Mobarry (LFM) model and snapshots of the MHD field lines projection on SM X-Z plane.

currents are mapped from this boundary to the ionosphere, where electric potential is solved. The solution for the potential then provides an electric field that is mapped back to the inner boundary where it is used as a boundary condition for the MHD evolution.

[11] In this study, the magnetosphere reconfiguration is driven by a southward turning of the interplanetary magnetic field (IMF), which is northward for an extended period of time. The IMF remains southward for 2 hours and then turns back to northward. Figure 2 shows the IMF history and snapshots of magnetic field lines projected into the SM X-Z plane. Solar wind velocity (V^{sw}) and density (n^{sw}) are kept constant during the simulation, with $V_x^{sw} = -400$ km·s^{-1}, $V_y^{sw} = V_z^{sw} = 0$, and $n^{sw} = 6.53$ cm^{-3}. The interplanetary magnetic field lines in Figure 2 are traced from the X axis at every 2 R_E. Geomagnetic field lines are traced from the model inner boundary on the noon-midnight meridian at every 3° starting from 48° latitude. As shown in Figure 2, the magnetosphere is closed after a long period of northward IMF (t_0). Then the southward turning of IMF starts reconnection on the dayside and open up of field lines at high latitudes (t_1). The magnetosphere gradually becomes longer and the plasma sheet is thinner (t_2). Between t_2 and t_3, reconnection has initiated in the magnetotail and an X-line is formed at about 25 R_E. Since then dipolarization takes place, field lines are closing up and the newly formed closed flux tubes convect earthward (t_4). The IMF then turns back to northward. The magnetosphere gradually returns to its initial state (t_5).

3.2. Solar Wind Inflow and Polar Wind, Auroral O^+ Outflow

[12] We initiate protons and O^+ from their representative source regions. The subsequent ion trajectories are calculated in the time-varying LFM fields using the test-particle code of *Delcourt et al.* [1993, 1994]. As per *Moore et al.* [2005], solar wind protons are initiated over the YZ plane at Xsm = 15 R_E. The source flux is constant with time and is equal to $n^{sw} \cdot V^{sw} = 2.6 \times 10^8$ cm^{-2} s^{-1}. Ions are released randomly in the thermal energy range of 0–10 eV, pitch angle range of 0–180°, gyro-phase angle range of 0–360° in the E × B frame from $t = -6$ hours to the end of the LFM run (t = 3 hours). Once the ions are initiated, they are picked up by the solar wind flow. We start at negative times such that ions have enough time to travel from the upstream region to the magnetosphere and well populate the magnetosphere at t = 0. The magnetosphere configuration at times less than zero is kept as that at t = 0. In total, 100 millions solar wind protons are released. Among them only a few percent enter into the magnetosphere. The rest of them just flow around the magnetosphere and are lost downstream.

[13] For polar wind, protons are released on a sphere of 4 R_E radii at magnetic latitudes above 55° with energy of 50–100 eV, all phase angles, pitch angle of 170°–180° in Northern Hemisphere and 0°–10° at south [*Moore et al.*, 2005]. Ions are initiated from −15 to 3 hours with a constant flux of 7.1 × 10^6 cm^{-2}s^{-1}. We have assumed polar wind escaping flux is relatively unaffected by auroral acceleration processes and geomagnetic activity [*Moore et al.*, 1999]. We start releasing polar wind protons (−15 hours) well before the start time of solar wind ions (−6 hours) because it takes longer time for low-energy polar wind ions to travel from the polar region to the magnetosphere. A total of 500,000 polar wind ions are released.

[14] For the auroral wind, 2 million O^+ are released from the topside ionosphere at 1000 km altitude from 60° to 90° latitude at both hemispheres from −15 to 3 hours. However, the O^+ source flux F, thermal energy E_{th}, and parallel energy $E_\parallel$ are driven by the local MHD parameters as follows:

$$F\left[\mathrm{cm}^{-2}\mathrm{s}^{-1}\right] = 10^9\left(0.1N_{\mathrm{mag}}\right)^{2.2} + 1.1 \times 10^8\ S_{1\mathrm{K}}^{1.26} \quad (1)$$

$$E_{\mathrm{th}}(\mathrm{eV}) = 0.1\mathrm{eV} + 1.6\ S_{1\mathrm{K}}^{1.26} \quad (2)$$

$$E_\parallel(\mathrm{eV}) = E_{\mathrm{th}} + e\Phi_\parallel \quad (3)$$

$$\text{where } \Phi_\parallel = 1500\left(J_\parallel - 0.33\right)^2 \quad \text{if } J_\parallel > 0.33\ \mu\mathrm{A/m}^2$$
$$\Phi_\parallel = 0 \quad \text{if } J_\parallel < 0.33\ \mu\mathrm{A/m}^2$$

N_{mag} is the magnetospheric density in cm^{-3} at the LFM inner boundary at 3.2 R_E. S_{1K} is the LFM ionospheric Joule heating in mW/m^2 mapped to 1000 km altitude. $\Phi_\parallel$ is the parallel potential drop, which is estimated as shown from the upward field-aligned current at the ionosphere. All of the physical parameters used in equation (1) are derived from observations. The outflow description comes from *Strangeway et al.* [2005] and *Zheng et al.* [2005]. They found the two primary energy sources of ion outflow are soft electron precipitation and dissipation of downward Poynting flux. In equation (1) we use magnetospheric density and Joule heating as proxies for electron precipitation and Poynting flux, respectively. The temperature dependence on Poynting flux shown in equation (2) is given by R. J. Strangeway (private communication, 2006). The parallel potential drops in equation (3) are based on the Knight-like relation given by *Lyons* [1981], based on the current systems from the global simulation. O^+ are released at randomly selected phase angles. Pitch angles are determined from E_{th} and $E_\parallel$.

[15] Figure 3 shows the MHD parameters and the corresponding auroral wind outflow parameters at 1000 km altitude at t = 0 and 52 min (t_0 and t_2 in Figure 2). In the plots, Sun is up, and magnetic latitudes of 60°, 70° and 80° are depicted. The magnetospheric density is mapped along dipole field lines from the LFM inner boundary to 1000 km altitude, assuming constant density along field lines. As shown in Figure 3, at t_0, the magnetospheric particle and energy sources for O^+ outflow are strongest on the dayside at high latitudes, where reconnection takes place. As a result the strongest outflow flux and energy are also located on dayside high-latitude region. At t_2 when the IMF has been southward for 52 min, strong outflow extends to lower latitudes and also to dawn and dusk local times. The highest O^+ parallel energy is found in the noon-dusk sector, where the parallel potential drop (upward field-aligned current) is the strongest. $\Phi_\parallel$ is strongest on the duskside because the sign of the vorticity in that boundary layer is preferentially such as to drive current upward from the ionosphere, yielding larger parallel potential drops needed to drive magnetospheric electrons into the ionosphere. However, these auroral features are indeed present in the evening as well as the dusk to afternoon hours, but are more transitory in association with the substorm. In fact, a clear westward traveling surge begins near midnight and moves toward the dusk region, producing a peak parallel potential drop of ∼ 1 kV at about 01:27 hrs into the simulation.

[16] The global O^+ fluence that our model yields for this simulation run ranges from 2 × 10^{25} to 8 × 10^{26} ion/s. The range given by *Yau et al.* [1988] in their Figure 4, from their statistical study for Dst between zero and −60 nT (the range matching our simulation results) and for F10.7 in the high range from 100–150, is 3 × 10^{25} to 2 × 10^{26} ion/s. Our simulation is for a single discrete substorm, so it is expected that our short-lived peak flux would exceed their statistical average somewhat. Our Polar Wind H^+ fluence (1 × 10^{26} ion/s) is in close agreement with the total H^+ fluence given by *Yau et al.* [1988] in the above cited figure.

3.3. Calculation of Density and Pressure in the Magnetosphere

[17] Similar to the approach in the work of *Moore et al.* [2005], the entire simulation domain (X = −70 to 15 R_E, Y = −30 to 30 R_E, Z = −30 to 30 R_E) is divided into volume elements of 1 R_E^3. In this dynamic case, we also divided the time in intervals of Δt. The density in volume

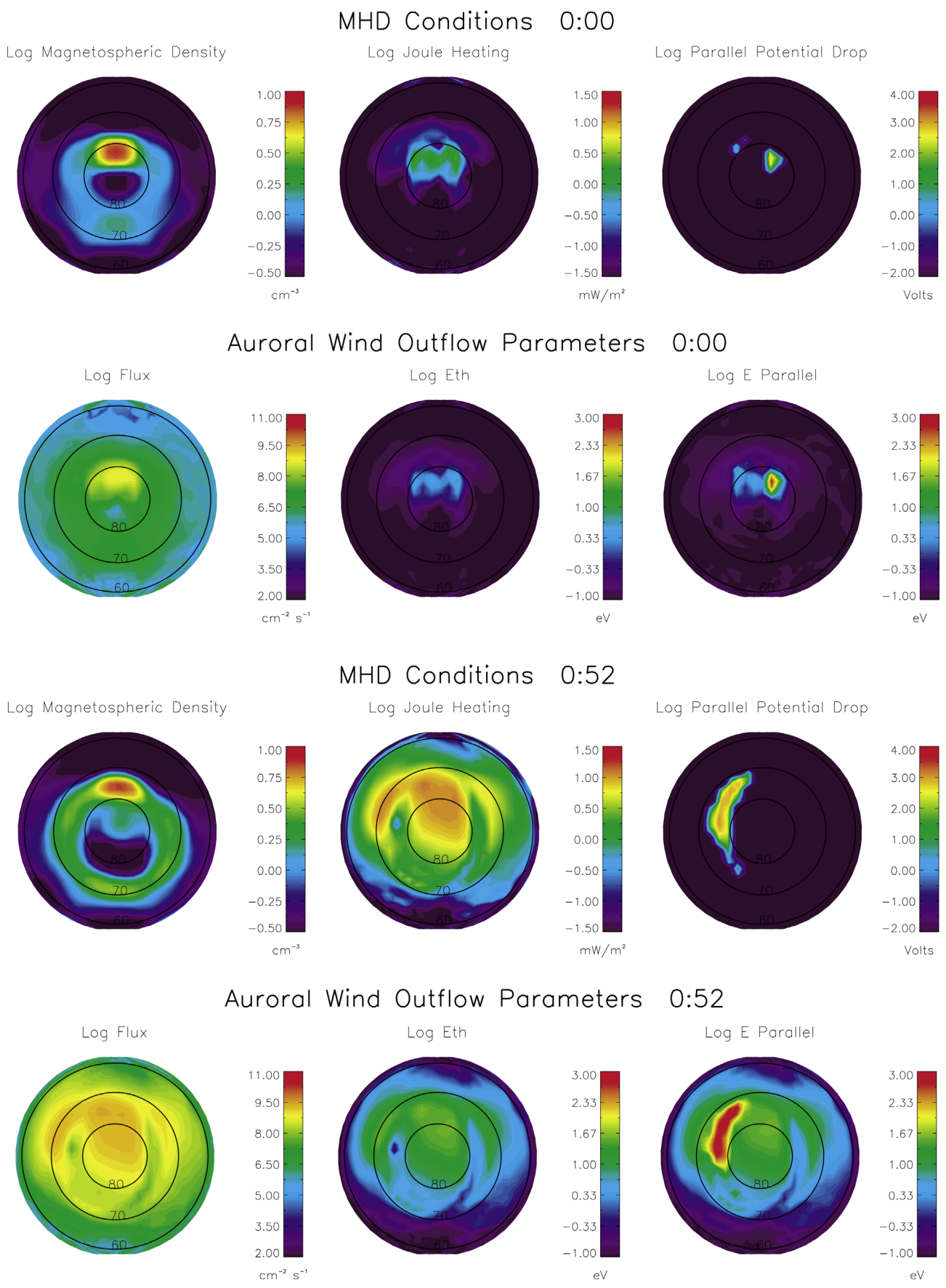

Figure 3. MHD conditions and auroral outflow parameters at 1000 km altitude at $t = 0$ and 52 min.

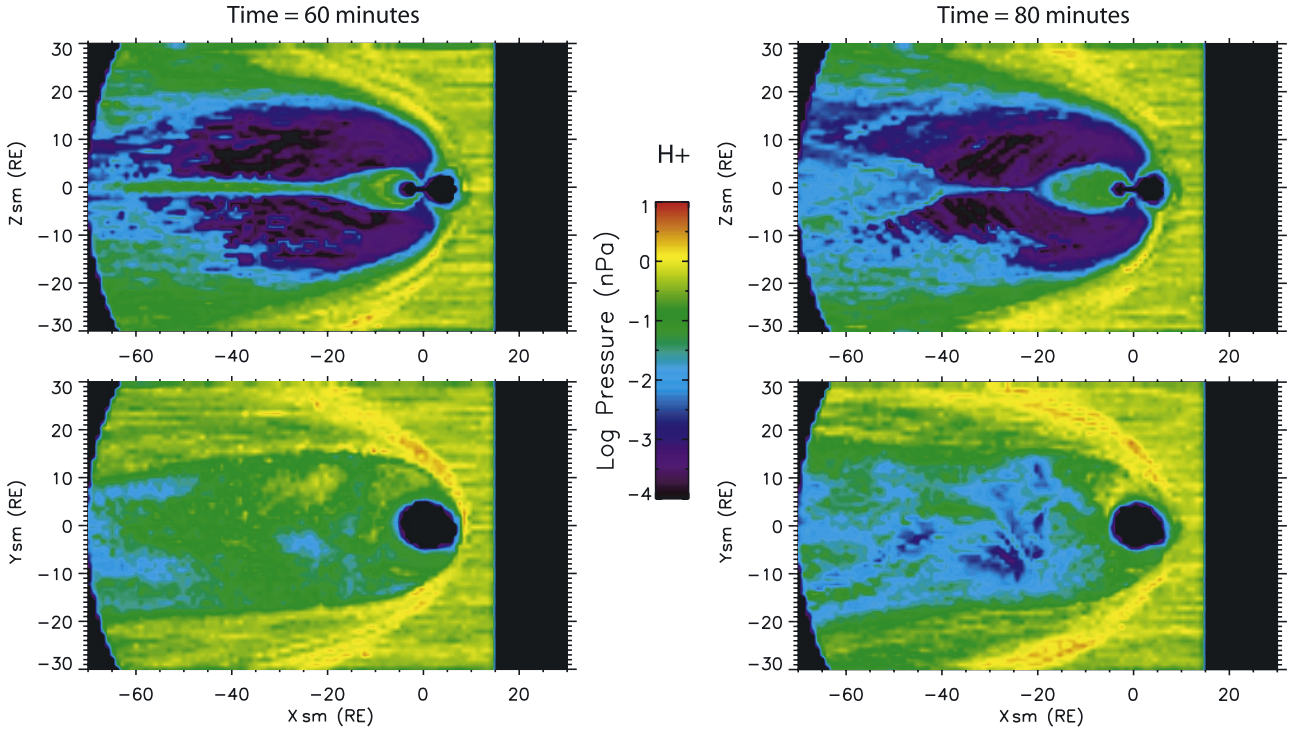

Figure 4. H^+ pressure on X-Z and X-Y planes at (left) 60 min and (right) 80 min.

bin j at time t contributed by particle i, which passes through bin j between $(t - 0.5\ \Delta t)$ and $(t + 0.5\ \Delta t)$, is given by

$$n_{ij}(t) = F_i(t_i)|\cos\alpha_i(t_i)|dA\frac{T_{ij}}{V_j}; dA = \frac{A}{N_{\Delta t}} \tag{4}$$

where F_i is the ion source flux, which is a function of t_i, the time particle i is launched, α_i is the initial pitch angle, dA is the area of the source surface allocated to each particle, that is the total source surface area, A, divided by number of particles launched in Δt ($N_{\Delta t}$), T_{ij} is residence time of particle i in bin j, and V_j is the volume of bin j, that is 1 R_E^3 in our case. Note that F_i and α_i in the auroral wind case depend on the time of ejection, t_i (Figure 3).

[18] The density in bin j at time t is just the summation of all particles that pass through bin j between $(t - 0.5\ \Delta t)$ and $(t + 0.5\ \Delta t)$:

$$n_j(t) = \sum_i n_{ij}(t) \tag{5}$$

Once densities are calculated, the total (dynamic plus kinetic) pressure at bin j is given by:

$$P_j(t) = \sum_i P_{ij}(t) = \frac{2}{3}\sum_i n_{ij}(t)E_{ij}(t) \tag{6}$$

where E_{ij} is the average energy of particle i in bin j.

3.4. Comprehensive Ring Current Model

[19] As described above, the ion density and pressure in the magnetosphere are established by tracking particle energies along their trajectories. However, the LFM model generally underestimates the electric field in the inner magnetosphere. This is a common problem of ideal MHD models. As a result, the test-particle calculation will underestimate the ion penetration into the ring current region and the ion fluxes there. To resolve this problem, we use the simulated ion density and mean energy at the inner plasma sheet as boundary conditions to a kinetic ring current model to calculate the ion distribution in the inner magnetosphere. The ring current model we employed is the Comprehensive Ring Current Model (CRCM) described by *Fok et al.* [2001]. The CRCM calculates the ring current ion fluxes and ionospheric potentials in a self-consistent manner. The two main equations solved by the CRCM are

$$\frac{\partial f_s}{\partial t} + \langle\dot{\lambda}_i\rangle\frac{\partial f_s}{\partial\lambda_i} + \langle\dot{\phi}_i\rangle\frac{\partial f_s}{\partial\phi_i} = -v\sigma_{sH}\langle n_H\rangle f_s - \left(\frac{f_s}{0.5\tau_b}\right)_{\text{losscone}} \tag{7}$$

$$\nabla\bullet\left(-\overleftrightarrow{\Sigma}\nabla\Phi\right) = J_\parallel\sin I \tag{8}$$

where f_s is distribution of ring current species s. λ_i and ϕ_i are the magnetic latitude and local time at the ionosphere, respectively. f_s is a function of λ_i, ϕ_i, first and second adiabatic invariants, and is assumed to be constant along a field line. Equatorial fluxes can be obtained by mapping f_s along field lines from the ionospheric grid to the equator. $\langle\dot{\lambda}_i\rangle$ and $\langle\dot{\phi}_i\rangle$ are the bounce-average velocities of species s on the ionospheric grid. σ_{sH} is charge exchange cross sections for the ring current species s with neutral H. $\langle n_H\rangle$ is the bounce-averaged neutral density of H. τ_b is bounce period. $\overleftrightarrow{\Sigma}$ is a tensor representing ionospheric Hall and Pedersen conductance. Φ and $J_\parallel$ are the ionospheric potential and field-aligned current. I is the magnetic dip

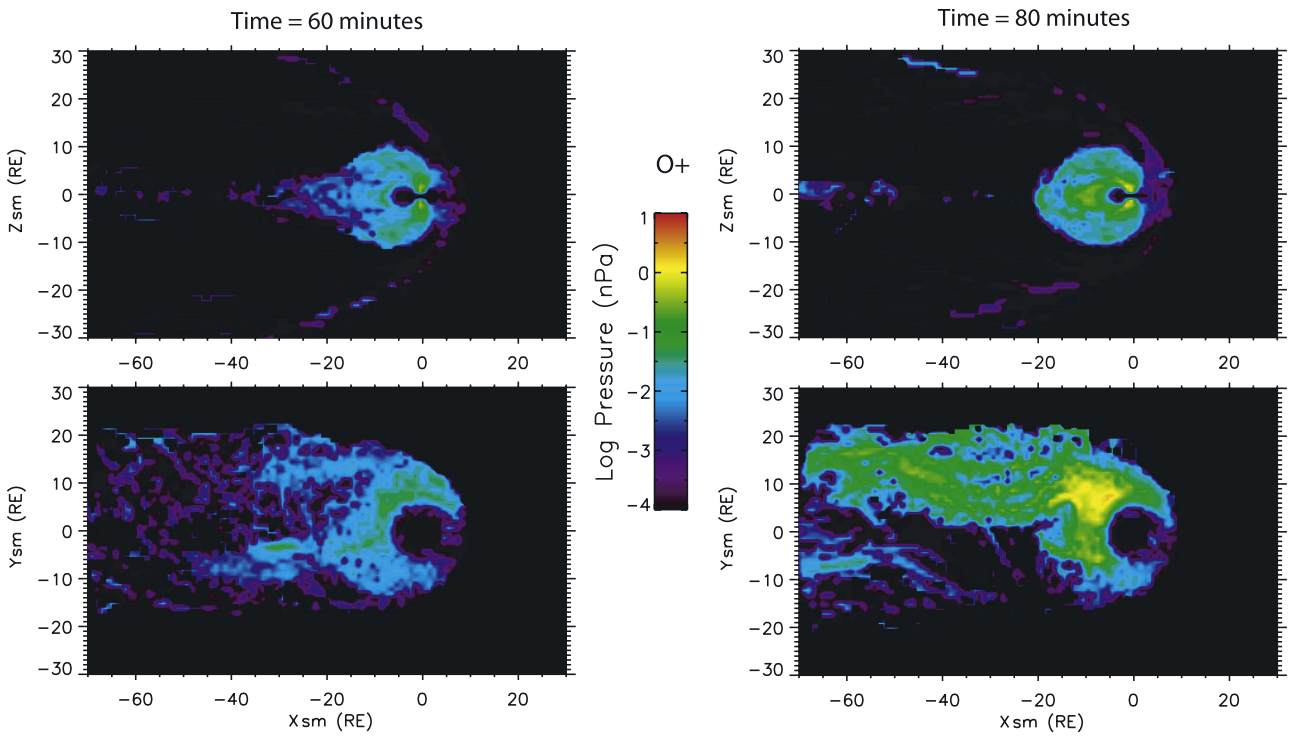

Figure 5. O^+ pressure on X-Z and X-Y planes at (left) 60 min and (right) 80 min.

angle. Equation (7) represents a drift-loss model of the ring current species s with the consideration of charge exchange and loss-cone losses. The ionospheric field-aligned current in equation (8) is calculated from the nonzero divergence of the perpendicular current contributed by all the ring current species. In this study, both ring current H^+ (originated from solar wind and polar wind) and O^+ (originating from auroral wind) are considered in the calculation of $J_{\|}$ in equation (8). This method produces improved simulation of the convection electric field and ring current strength in the inner magnetosphere, as described below.

4. Simulation Results

4.1. Pressure Enhancement in the Plasma Sheet

[20] We calculate the proton and O^+ pressure in the entire simulation domain during the event as described in section 3.3. Figure 4 shows the proton (solar wind plus polar wind) pressure on X-Z and X-Y planes at 60 and 80 min after the IMF southward turning. In both cases, the lobes are occupied by polar wind plasma while the plasma sheet is a mixture of polar and solar particles. At 60 min (left panels) when substorm onset has just commenced, thin plasma sheet was developed. As dipolarization continues, 20 min later (right panels), the lobes are well filled with polar wind ions. At the same time, a plasmoid is formed and is streaming tailward. At this time, a pressure peak is found at $\sim$10 R_E in the dusk-midnight sector. These are protons being energized and drift earthward from the plasma sheet during substorm expansion.

[21] Figure 5 shows the simulated O^+ pressure at the same times as shown in Figure 4. At 60 min (left panels) at the substorm onset, high O^+ pressure is observed in the near-Earth lobe and plasma sheet regions. The blob seen on the equatorial plane on the dawnside at $\sim$30 R_E is the high pressure from the tailward streaming O^+ away from the newly formed reconnection X line. Twenty minutes later (right panels), the high-pressure region extended to low latitudes and to the duskside plasmas sheet. The high pressure on the duskside of the plasma sheet for $x < -20$ R_E is coming from strong outflow parallel energy in the ionospheric source region during the growth phase (bottom-right panel, Figure 3). A strong pressure peak is seen at the equatorial plane at $\sim$2100 MLT at 12 R_E. These are particles flowing earthward from the reconnection region or particles energized locally by dipolarization. Both the proton and O^+ peaks are located in the dusk-midnight sector. However, the O^+ enhancement is stronger and extends to broader region.

[22] In order to understand why the O^+ pressure increases significantly during substorm dipolarization, we examine individual O^+ trajectories and their energy changes during the event. Figure 6 plots the trajectory of an auroral O^+, which passes through the pressure peak at 80 min as shown in Figure 5. Particle trajectory is projected on the X-Z and X-Y plane and the trace is painted by the instantaneous ion energy. The lower four panels of Figure 6 plot the temporal variation of ion total energy, parallel energy, perpendicular energy, and magnetic moment, which is normalized by the initial value. This oxygen ion is released at $\sim$zero hour. The initial energy is 18 eV. The ion travels along the field line until it is picked up by the strong convection during southward IMF. It then convects antisunward to the plasma sheet. By the time ($\sim$ 80 min) the ion comes close to the plasma sheet, substorm onset has been triggered. Fast MHD earthward flow during substorm expansion pushes field lines and the ion inward and simultaneously energizes it sharply to almost 2 orders of magnitude increase in energy. This fast MHD flow is equivalent to the strong inductive

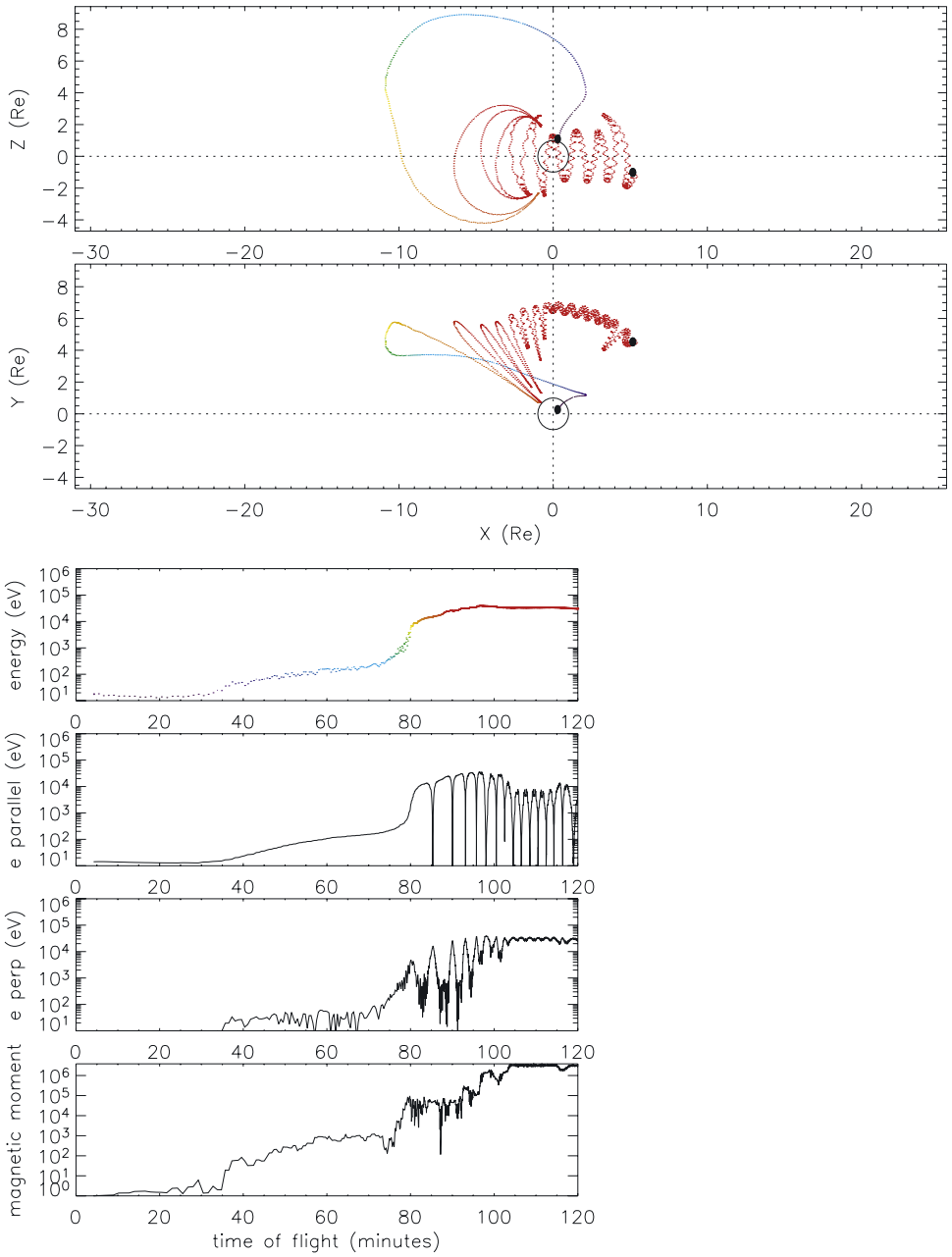

Figure 6. O^+ trajectory projected on X-Z and X-Y planes. The lower two panels are ion energy and normalized magnetic moment during the time of flight.

electric field in electromagnetic theory during magnetic reconfiguration. Both the O^+ parallel and perpendicular energy grow sharply at this time. The magnetic moment also increases in a similar way, indicating the energization process is highly nonadiabatic. It is evident that the gyroperiod of the heavy ion is comparable with the timescale of the field variation so that the adiabaticity of magnetic moment is violated. We do not show in Figure 6 the variation of the second adiabatic invariant because it is difficult to compute. In fact, the violation of the second invariant occurs before the first invariant does owning to the longer timescale associated with bounce motion than gyration. The large increase in parallel energy as shown in Figure 6 implies serious violation of the second invariant. When the ion encounters the high-B region, because of the large energy acquired, it starts gradient-curvature drift to the dusk sector.

4.2. Flux Enhancements in the Ring Current Region

[23] The pressure enhancements seen in the near-Earth plasma sheet after substorm onset (Figures 5 and 6) in theory should propagate inward to the ring current region. However, as mentioned above, the convection electric field in the inner magnetosphere predicted by the LFM model is weaker than it should be. Therefore, using the test-particle-MHD approach could not reproduce flux enhancement in

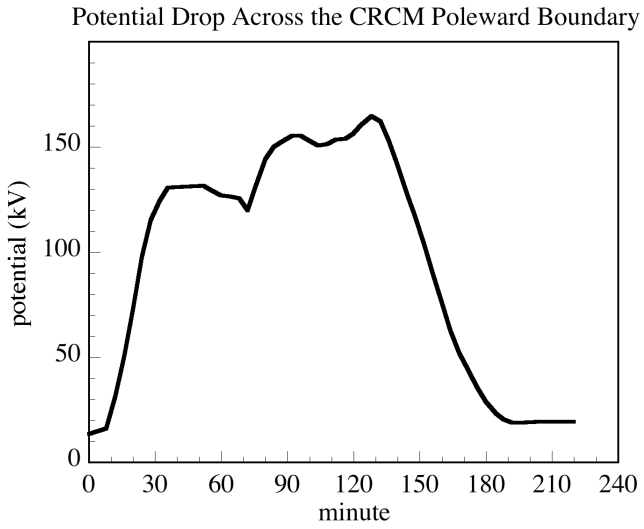

Figure 7. Potential drop in kV across the Comprehensive Ring Current Model (CRCM) poleward at the ionosphere.

the ring current often seen during storms and substorms. To resolve this problem, we calculate the ion distributions in the inner magnetosphere (Ro < 8 R_E) using the CRCM. The potential drop across the CRCM poleward boundary at 68.4° latitude in the ionosphere is taken from the LFM output (Figure 7). The test-particle-LFM results (density and mean energy) are used to specify the CRCM boundary condition at the equator at 8 R_E. Equation (7) is then solved with the magnetic field specified by the LFM model and electric field (potential) calculated from equation (8). Figure 8 shows the CRCM boundary condition (H^+, O^+ density and mean energy) at the equator at 8 R_E at the time of 64 min, which are calculated using the approach described in section 3.3. The distribution at the boundary is assumed to be a bi-Maxwellian ($T_{\parallel} \neq T_{\perp}$). It can be seen in Figure 8 that at this time during the substorm expansion, H^+ (mixture of polar and solar wind particles) at 8 R_E is denser but colder than O^+. Moreover, the H^+ temperatures are pretty isotropic but noticeable anisotropy in O^+ temperatures is seen, especially in the dusk-midnight sector. The O^+ parallel energy is higher than the perpendicular energy, indicating that O^+ energization is preferential in the parallel direction in that region. Field-aligned distribution has been observed at the geosynchronous orbit [*Mauk and McIlwain*, 1975] and is reproduced by test-particle simulations of *Delcourt* [2002] and *Mauk* [1986]. The strong acceleration in the field-aligned direction is associated with the violation of the second adiabatic invariant [*Mauk*, 1986]. For a given energy, the bounce period of O^+ is longer than that of H^+ so that in some cases, the second adiabatic invariant of O^+ is not conserved while it is conserved for H^+.

[24] We run the CRCM throughout the event with magnetic field updated every 5 min and boundary flux at 8 R_E updated every 4 min. The initial distributions of H^+ and O^+ are taken from the quiet time distribution measured by the

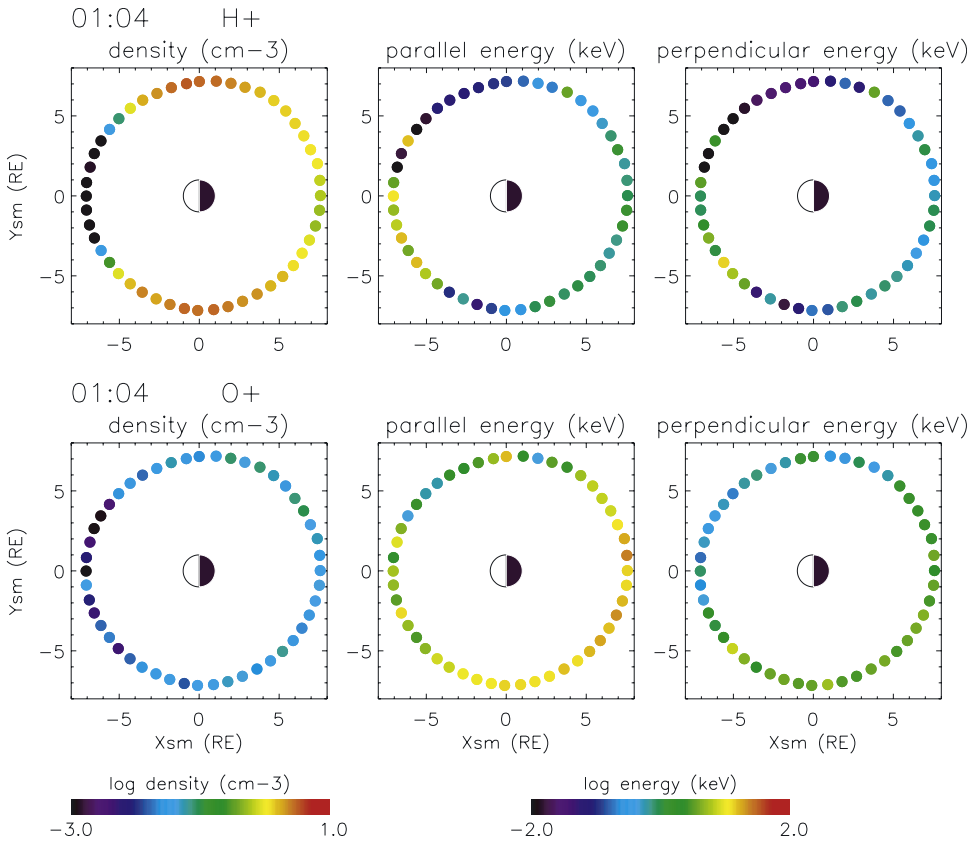

Figure 8. CRCM boundary densities and mean energies of (top) H^+ and (bottom) O^+, at 8 R_E equatorial distance at time = 64 min, calculated from the test-particle-LFM models.

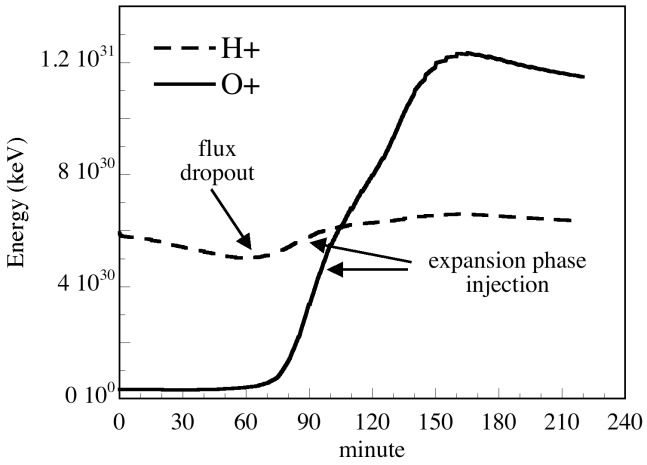

Figure 9. H^+ (dashed line) and O^+ (solid line) total energies inside 8 R_E during the substorm event.

Active Magnetospheric Particle Tracer Explorers (AMPTE)/ Charge Composition Explorer (CCE) spacecraft [*Sheldon and Hamilton*, 1993]. Figure 9 plots the temporal variations of H^+ and O^+ total energies inside 8 R_E. At the beginning during quiet time, H^+ energy content is much higher than O^+. This is consistent with observations that H^+ is the dominant species at quiet times [*Young et al.*, 1982; *Hamilton et al.*, 1988]. In the first hour before the onset, both energies are fairly constant with time. A slightly decrease in H^+ energy is seen in this hour. This decrease in particle energy (or flux) is known as flux dropout during substorm growth phase [*Baker and McPherron*, 1990; *Sauvaud et al.*, 1996]. The O^+ energy does not show such dropout owing to the strong outflow during the growth phase. After the substorm onset at ~60 min, both H^+ and O^+ total energies increase. However, the O^+ energy increases much faster than that of H^+. At ~100 min, the O^+ energy exceeds that of the H^+ and is kept rising even after the northward turning of the IMF at 120 min. The faster energy increase of O^+ than H^+ comes from the fact that there are higher O^+ particle and energy influxes at the CRCM model boundary. All ions are continually accelerated in the ring current region by the convection. However, the ratio of energy gain $\Delta E_O^+/\Delta E_H^+$ in the ring current is predominantly determined by the boundary distributions, which are controlled by energization processes in the plasma sheet. The total energy of H^+ and O^+ in the ring current region ($r < 8\,R_E$) at 160 min are 1.9×10^{31} keV, which would produce a surface magnetic depression of 75 nT [*Dessler and Parker*, 1959; *Sckopke*, 1966].

[25] As shown in section 2, IMAGE/HENA observes quick rise and decay of oxygen ENA during substorms. Our simulations also show large increase in O^+ flux in response to substorm expansion. It is interesting to see whether our simulation reproduces the observed oxygen ENA signatures during a substorm. Figure 10 (upper panels) shows the HENA 50–180 keV O images at three times during the substorm on 28 October 2001, the same substorm we discussed in section 2. Figure 10a is the image taken at early substorm expansion, Figure 10b is late expansion, and Figure 10c is in the recovery phase. The bottom panels of Figure 10 are the CRCM simulated equatorial O^+ flux also at the beginning, at the peak of substorm injection, and during the recovery. The corresponding O ENA emissions are depicted in the middle panels. Arrows are placed in the top and middle panels of Figure 10 to highlight the similarities between observations and simulations. At the early expansion phase (Figure 10, left panels), the simulated injection boundary (the earthward edge of the injected plasma cloud) is located at ~5 R_E. At this time both the HENA data and simulated ENA image show soft enhancements at high altitudes (arrows). The ENA emissions near the Earth are produced from ions with mirror points at low altitudes. Note that the ion pitch-angle distribution is field-aligned and neutral hydrogen density increases with decreasing altitude. The combined effects yield a stronger emission at low altitudes. As the event continues (Figure 10, middle panels), the simulated injection boundary moves inward to the ~ 3 R_E. Both simulated and observed ENA images show strong fluxes at low altitudes. Again these strong emissions are coming from charge exchange loss of field-aligned ions. In addition to the strong emission near the Earth, there is a local maximum at high altitudes in the dusk-midnight sector. The emissions here are from ions that are mirroring near the equator. This second ENA peak is more obvious in the simulated image than in the observed one. During the recovery of the substorm (Figure 10, right panels), the convection strength subsides. The injected oxygen ions drift westward to the dayside. As a consequence, strong ENA emissions are found on the dayside in both the simulation and HENA data.

[26] Although our LFM-Delcourt-CRCM simulation reproduces qualitatively the observed oxygen ENA features during a substorm, there are quantitative differences between the model and data. For this particular substorm the 28 October 2001, it takes 21 min (Figure 10, upper panels) from the initiation of ENA enhancement to its maximum and 35 min from peak emission to substantial decay. The timescales in the simulation are longer (44 and 52 min). The discrepancy in timing may come from the fact that the LFM substorm presented here is not as strong as the one on 28 October 2001. The southward IMF in the LFM simulation is only 5 nT. With a more negative IMF Bz, the transition between different phases of the substorm would be faster. Strong southward IMF would also produce strong convection that pushes ions deeper inward and shortens the decay lifetimes. Another noticeable difference between the HENA and the simulated O fluxes is that HENA images exhibit spatially smoother emissions than the simulation. However, one should keep in mind the angular-scattering problem in the HENA oxygen data (see section 2) when comparing simulated oxygen ENA fluxes with HENA images. The two-band structure in oxygen ENA emission predicted by the CRCM (Figure 10, middle panels) may be blurred out in the HENA data owing to scattering at the instrument front foil.

5. Discussion

[27] It is well known that the O^+/H^+ ratio increases during magnetic storms and substorms [*Young et al.*, 1982; *Hamilton et al.*, 1988; *Roeder et al.*, 1996; *Daglis*, 1997; *Mitchell et al.*, 2003; *Nose et al.*, 2005]. The simulations presented in this paper provide quantitative assessment on

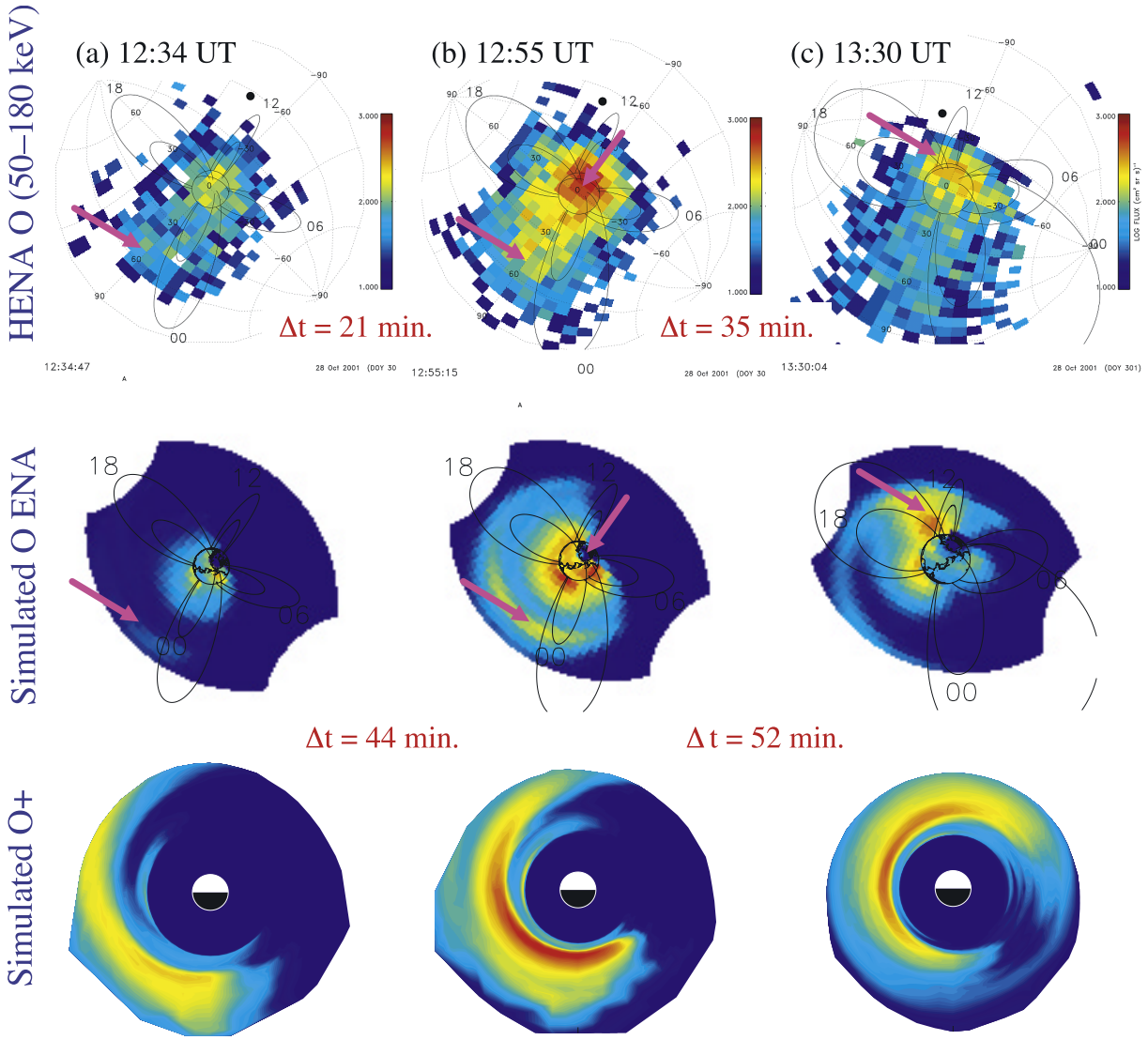

Figure 10. (top) HENA 50–180 keV O images at three times during a substorm on 28 October 2001. (middle) Simulated O ENA emissions. (bottom) Simulated equatorial O^+ fluxes.

storm and substorm processes that are accountable for the increase of the O^+/H^+ ratio. During storm times when convection are strong, magnetospheric energy dissipated into the ionosphere in the forms of enhanced particle precipitation, Joule heating and parallel potential drop. All these processes stimulate the up flowing of ionospheric O^+ (Figure 3). Magnetospheric energy input to the ionosphere also rises during substorms and causes the increase of O^+ outflow. However, there is a time lag (tens of minutes) between enhanced ionospheric outflow and resulting enhanced pressure in the magnetosphere. In addition to enhanced O^+ outflow, the inductive electric field associated with substorm magnetic reconfiguration in the magnetotail energizes the preexisted O^+ in a highly nonadiabatic manner. This substorm-associated energization produces rapid intensification of heavy ions without noticeable time lag. On the other hand, H^+ is found to be less susceptible to storm and substorm activity [*Kistler et al.*, 2005]. As a result, O^+/H^+ ratio increases with increasing geomagnetic activity. In this study, we found the O^+ energy content in the ring current is higher than that of H^+ (Figure 9) for a storm size of Dst $\sim$ 75 nT only. We may have overestimated the O^+ up flowing fluxes (equations (1)–(3)). Further improvement and refinement will be implemented in our auroral outflow model for future works.

[28] IMAGE/HENA observed instant response of oxygen ENA to substorm expansion [*Mitchell et al.*, 2003]. A burst of oxygen ENA is seen at the time of auroral brightening (Figure 1). The source of this O^+ enhancement is not fully determined yet. Two potential candidates are: direct injection of O^+ from the ionosphere [*Sheldon et al.*, 1998] and energization of the preexisting O^+ [*Delcourt*, 2002]. *Sheldon et al.* [1998] observed a O^+ enriched field-aligned beam at $\sim$40 keV from particle detector on the Polar satellite. This population existed from L = 3–7 for a duration of longer than 2 hours. Thus this long-lived field-aligned signature is not the same bursty feature seen by IMAGE/HENA during substorms. Upgoing oxygen ions are also seen routinely from FAST (J. U. Kozyra, private communication, 2006), CRRES [*Rubin et al.*, 1995] satel-

lites. However, the energies of the upflowing ions are below one keV. For direct-injection mechanism, the energy of the outflow ions must be high enough (> few keVs) such that the bounce time is comparable with substorm expansion timescale of minutes. Our simulation results support the mechanism of energization of preexisting ions in the magnetosphere. As shown in Figure 6, it takes more than an hour for the oxygen ion (initial energy = 62 eV) to convect from the dayside to the nightside. However, the ion arrives at the plasma sheet when dipolarization is taking place. The energy of the ion then sharply increases in 2 orders of magnitude to $\sim$ 100 keV in just a minute. After reaching high energy, the ion drifts westward to the dusk sector, where O^+ pressure peak is established (lower right panel, Figure 5). In summary, direct injection of energetic O^+ is seldom observed. Our simulations show energization of preexisting O^+ alone could produce the observed substorm O^+ bursts.

[29] We have shown in Figure 8 that O^+ ions tend to have field-aligned distribution in the plasma sheet during dipolarization. This field-aligned feature during substorms is consistent with the simulation results of *Mauk* [1986] and ion measurements at the geosynchronous orbit presented by *Mauk and McIlwain* [1975]. However, some other observational and test-particle simulation studies found perpendicular pitch angle distribution of O^+ ions after substorm onset [*Lui*, 1996; *Nose et al.*, 2000; *Sanchez et al.*, 1993]. The discrepancy between these two findings may come from the timescale of the substorm reconfiguration. If at the point where dipolarization is fast and both the first and second adiabatic invariants are violated, ions at that location are accelerated preferentially in the perpendicular direction. At the locations where dipolarization is relatively slow such that the first invariant is conserved but the second invariant is not, ions are primarily energized in the parallel direction. The LFM substorm we present here is a comparatively weak and slow substorm. The majority of the O^+ ions experience less violation of the magnetic moment than the violation of the second invariant. As a result, field-aligned distribution is found in the dipolarization region.

[30] Energization of preexisting ion mechanism can also explain the short-lived nature of the substorm O^+ bursts. We have shown the field-aligned characteristics of substorm O^+ (Figure 8) owing to the violation of the second adiabatic invariant during the acceleration process. Field-aligned ions with mirror points at low altitudes will encounter the dense neutral atmosphere and experience stronger collisional losses. The anisotropic ion distribution also stimulates wave growth that diffuses ions into the loss cone. If wave loss is included in our calculation, the decay time will be further shortened and has better agreement with the HENA data.

6. Summary

[31] IMAGE/HENA observes rapid rise of high-energy (50–180 keV) oxygen ENA during substorm expansions and fast decay in the recovery phases. On the other hand, the hydrogen ENA emissions are relatively stable during substorms. We have performed a series of simulation to understand the physics controlling the growth and decay of O^+ and H^+ during a substorm. The LFM model is used to model a substorm that is triggered by a constant southward IMF of 5 nT. Using a test-particle code we launch millions of ions in the LFM fields from the solar wind, polar wind and auroral wind source regions hours before and throughout the event. Ion density, parallel and perpendicular temperatures are calculated at the equator at 8 R_E. These ion distributions are used as boundary conditions for the CRCM to calculate the detailed energy spectra of ring current H^+ and O^+. The corresponding ENA fluxes are computed and compared with the HENA substorm data on 28 October 2001. We found the following:

[32] 1. The simulation shows a rapid increase in O+ pressure in the plasma sheet during the substorm expansion. The changes in H+ pressure are relatively weak.

[33] 2. The calculated O+/H+ energy ratio in the ring current region increases with increasing geomagnetic activity, consistent with observations.

[34] 3. The simulated O ENA emissions reproduce some observable substorm signatures from IMAGE/HENA but the calculated ENA growth and decay timescales are longer than observations.

[35] 4. From our simulations and HENA observations, it appears that O+ bursts seen during substorms can be explained by nonadiabatic energization of preexisting O+, without the contribution from direct injection of ionospheric ions.

[36] 5. The calculated O+ enhancements are found to have pitch angles favoring the field-aligned direction. This pitch-angle distribution partly explains the rapid decay of the observed substorm O+ bursts.

[37] **Acknowledgments.** We would like to thank Manuel Buenfil for performing the test-particle and bulk parameters calculations. This research is funded by the NASA Science Mission Directorate, Earth-Sun System Guest Investigator Program, under RTOP grant 370-16-10-11. Research at JHU/APL is funded by NASA grant NAG5-12722 and NSF grant ATM-0302529.

[38] Wolfgang Baumjohann thanks Masahito Nose and another reviewer for their assistance in evaluating this manuscript.

References

Baker, D. N., and R. L. McPherron (1990), Extreme energetic particle decreases near geostationary orbit: A manifestation of current diversion within the inner plasma sheet, *J. Geophys. Res.*, *95*, 6591–6599.

Baker, D. N., E. W. Hone Jr., D. T. Young, and J. Birn (1982), The possible role of ionospheric oxygen in the initiation and development of plasma sheet instabilities, *Geophys. Res. Lett.*, *9*, 1337–1340.

Baker, D. N., T. A. Fritz, W. Lennartsson, B. Wiken, H. W. Kroehl, and J. Birn (1985), The role of heavy ionospheric ions in the localization of substorm disturbances on March 22, 1979: CDAW 6, *J. Geophys. Res.*, *90*, 1273–1281.

Brandt, P. C:son, S. Ohtani, D. G. Mitchell, M.-C. Fok, E. C. Roelof, and R. Demajistre (2002), Global ENA observations of the storm mainphase ring current: Implications for skewed electric fields in the inner magnetosphere, *Geophys. Res. Lett.*, *29*(20), 1954, doi:10.1029/2002GL015160.

Daglis, I. A. (1997), The role of magnetosphere-ionosphere coupling in magnetic storm dynamics, in *Magnetic Storm*, *Geophys. Monogr. Ser.*, vol. 98, edited by B. T. Tsurutani et al., pp. 107–116, AGU, Washington, D. C.

Daglis, I. A., and W. L. Axford (1996), Fast ionospheric response to enhanced activity in geospace: Ion feeding of the inner magnetotail, *J. Geophys. Res.*, *101*, 5047–5065.

Delcourt, D. C. (2002), Particle acceleration by inductive electric fields in the inner magnetosphere, *J. Atmos. Sol. Terr. Phys.*, *64*, 551–559.

Delcourt, D. C., J. A. Sauvaud, and T. E. Moore (1993), Polar wind ion dynamics in the magnetotail, *J. Geophys. Res.*, *98*, 9155–9169.

Delcourt, D. C., T. E. Moore, and C. R. Chappell (1994), Contribution of low-energy ionospheric protons to the plasma sheet, *J. Geophys. Res.*, *99*, 5681–5689.

Dessler, A. J., and E. N. Parker (1959), Hydromagnetic theory of geomagnetic storms, *J. Geophys. Res.*, *64*, 2239–2252.

Ebihara, Y., and M.-C. Fok (2004), Post-midnight storm-time enhancement of ten-of-keV proton flux, *J. Geophys. Res.*, *109*, A12209, doi:10.1029/2004JA010523.

Fedder, J. A., J. G. Lyon, S. P. Slinker, and C. M. Mobarry (1995), Topological structure of the magnetotail as a function of interplanetary magnetic field direction, *J. Geophys. Res.*, *100*, 3613–3621.

Fok, M.-C., R. A. Wolf, R. W. Spiro, and T. E. Moore (2001), Comprehensive computational model of the Earth's ring current, *J. Geophys. Res.*, *106*, 8417–8424.

Fok, M.-C., et al. (2003), Global ENA IMAGE simulations, *Space Sci. Rev.*, *109*, 77–103.

Hamilton, D. C., G. Gloeckler, F. M. Ipavich, W. Studemann, B. Wilken, and G. Kremser (1988), Ring current development during the great geomagnetic storm of February 86, *J. Geophys. Res.*, *93*, 14,343–14,355.

Kistler, L. M., et al. (2005), Contribution of nonadiabatic ions to the cross-tail current in an O+ dominated thin current sheet, *J. Geophys. Res.*, *110*, A06213, doi:10.1029/2004JA010653.

Lui, A. T. Y. (1996), Current disruption in the Earth's magnetosphere: Observations and models, *J. Geophys. Rev.*, *101*, 13,067–13,088.

Lyons, L. R. (1981), The field-aligned current versus electric potential relation and auroral electrodynamics, in *Physics of Auroral Arc Formation*, *Geophys. Monogr. Ser.*, vol. 25, edited by S. I. Akasofu and J. R. Kan, pp. 252–259, AGU, Washington, D. C.

Mauk, B. H. (1986), Quantitative modeling of the ''convection surge'' mechanism of ion acceleration, *J. Geophys. Res.*, *91*, 13,423–13,431.

Mauk, B. H., and C. E. McIlwain (1975), UCSD auroral particles experiment, *IEEE Trans. Aerosp. Electron. Syst.*, *AES-11*, 1125–1130.

Mende, S. B., et al. (2000), Far ultraviolet imaging from the IMAGE spacecraft, 2, Wideband FUV imaging, *Space Sci. Rev.*, *91*, 271–285.

Mitchell, D. G., et al. (2000), High energy neutral atom (HENA) imager for the IMAGE mission, *Space Sci. Rev.*, *91*, 67–112.

Mitchell, D. G., P. C:son Brandt, E. C. Roelof, D. C. Hamilton, K. Retterer, and S. Mende (2003), Global imaging of O^+ from IMAGE/HENA, *Space Sci. Rev.*, *109*, 63–75.

Mobarry, C. M., J. A. Fedder, and J. G. Lyon (1996), Equatorial plasma convection from global simulations of the Earth's magnetosphere, *J. Geophys. Res.*, *101*, 7859–7874.

Mobius, M., M. Scholer, B. Klecker, D. Hovestadt, G. Gloeckler, and F. M. Ipavich (1987), Acceleration of ions of ionospheric origin in the plasma sheet during substorm activity, in *Magnetotail Physics*, edited by A. T. Y. Lui, pp. 231–234, Johns Hopkins Univ. Press, Baltimore, Md.

Moore, T. E., and D. C. Delcourt (1995), The geopause, *Rev. Geophys*, *33*, 175–209.

Moore, T. E., R. Lundin, D. Alcayde, M. Andre, S. B. Ganguli, M. Temerin, and A. Yau (1999), Source processes in the high latitude ionosphere, *Space Sci. Rev.*, *88*(1–2), 7–88.

Moore, T. E., M. O. Chandler, M.-C. Fok, B. L. Giles, D. C. Delcourt, J. L. Horwitz, and C. J. Pollock (2001), Ring current and internal plasma sources, *Space Sci. Rev.*, *95*, 555–568.

Moore, T. E., M.-C. Fok, S. P. Christon, S.-H. Chen, M. O. Chandler, D. C. Delcourt, J. Fedder, S. Slinker, and M. Liemohn (2005), Solar and ionospheric plasmas in the ring current region, in *Inner Magnetosphere Interactions: New Perspectives from Imaging*, *Geophys. Monogr. Ser.*, vol. 159, edited by J. Burch et al., pp. 179–220, AGU, Washington, D. C.

Moore, T. E., M.-C. Fok, D. C. Delcourt, S. P. Slinker, and J. A. Fedder (2006), Global aspects of solar wind–ionosphere interactions, *J. Atmos. Sol. Terr. Phys.*, in press.

Nose, M., A. T. Y. Lui, S. Ohtani, B. H. Mauk, R. W. McEntire, D. J. Williams, T. Mukai, and K. Yumoto (2000), Acceleration of oxygen ions of ionospheric origin in the near-Earth magnetotail during substorms, *J. Geophys. Res.*, *105*, 7669–7677.

Nose, M., S. Taguchi, K. Hosokawa, S. P. Christon, R. W. McEntire, T. E. Moore, and M. R. Collier (2005), Overwhelming O^+ contribution to the plasma sheet energy density during the October 2003 superstorm: Geotail/EPIC and IMAGE/LENA observations, *J. Geophys. Res.*, *110*, A09S24, doi:10.1029/2004JA010930.

Roeder, J. L., J. F. Fennell, M. W. Chen, M. Schulz, M. Grande, and S. Livi (1996), CRRES observations of the composition of the ring-current ion populations, *Adv. Space Res.*, *17*(10), 17–24.

Roelof, E. C. (1997), ENA emission from nearly-mirroring magnetospheric ions interacting with the exosphere, *Adv. Space Res.*, *20*, 361–366.

Rubin, A. G., W. J. Burke, and D. A. Hardy (1995), Low-energy ion spectral peaks detected by CRRES in the plasma sheet, *J. Geophys. Res.*, *100*, 19,221–19,226.

Sanchez, E. R., B. H. Mauk, and C.-I. Meng (1993), Adiabatic vs. non-adiabatic particle distributions during convection surges, *Geophys. Res. Lett.*, *20*, 177–180.

Sauvaud, J. A., T. Beutier, and D. Delcourt (1996), On the origin of flux dropouts near geosynchronous orbit during the growth phase of substorms, 1, Betatron effects, *J. Geophys. Res.*, *101*, 19,911–19,919.

Sckopke, N. (1966), A general relation between the energy of trapped particles and the disturbance field near the Earth, *J. Geophys. Res.*, *71*, 3125–3130.

Sheldon, R. B., and D. C. Hamilton (1993), Ion transport and loss in the Earth's quiet ring current, 1, Data and standard model, *J. Geophys. Res.*, *98*, 13,491–13,508.

Sheldon, R. B., H. E. Spence, and J. F. Fennell (1998), Observation of 40 keV field-aligned ion beams, *Geophys. Res. Lett.*, *25*, 1617–1620.

Slinker, S. P., J. A. Fedder, J. Chen, and J. G. Lyon (1998), Global MHD simulation of the magnetosphere and ionosphere for 1930–2330 UT on November 3, 1993, *J. Geophys. Res.*, *103*, 26,243–26,250.

Slinker, S. P., J. A. Fedder, J. M. Ruohoniemi, and J. G. Lyon (2001), Global MHD simulation of the magnetosphere for November 24, 1996, *J. Geophys. Res.*, *106*, 361–380.

Strangeway, R. J., R. E. Ergun, Y.-J. Su, C. W. Carlson, and R. C. Elphic (2005), Factors controlling ionospheric outflows as observed at intermediate altitudes, *J. Geophys. Res.*, *110*, A03221, doi:10.1029/2004JA010829.

Winglee, R. M., D. Chua, M. Brittnacher, and G. K. Parks (2002), Global impact of ionospheric outflows on the dynamics of the magnetosphere and cross-polar cap potential, *J. Geophys. Res.*, *107*(A9), 1237, doi:10.1029/2001JA000214.

Yau, A. W., W. K. Peterson, and E. G. Shelley (1988), Quantitative parameterization of energetic ionospheric ion outflow, in *Modeling Magnetospheric Plasmas*, *Geophys. Monogr. Ser.*, vol. 44, pp. 211–271, AGU, Washington, D. C.

Young, D. T., H. Balsiger, and J. Geiss (1982), Correlations of magnetospheric ion composition with geomagnetic and solar activity, *J. Geophys. Res.*, *87*, 9077–9096.

Zheng, Y., T. E. Moore, F. S. Mozer, C. T. Russell, and R. J. Strangeway (2005), Polar study of ionospheric ion outflow versus energy input, *J. Geophys. Res.*, *110*, A07210, doi:10.1029/2004JA010995.

P. C. Brandt, Johns Hopkins University Applied Physics Laboratory, Laurel, MD 20723, USA.

D. C. Delcourt, CETP-Observatoire de Saint-Maur, 4 avenue de Neptune, 94107 Saint-Maur des Fosses, France.

J. A. Fedder, Leading Edge Technology, Inc., 1806 Rampart Drive, Alexandria, VA 22308, USA.

M.-C. Fok and T. E. Moore, NASA Goddard Space Flight Center, Code 673, Greenbelt, MD 20771, USA. (mei-ching.h.fok@nasa.gov)

S. P. Slinker, Naval Research Laboratory, Washington, DC, 20375, USA.